

# Motion from Shape Change

OLIVER GROSS, TU Berlin, Germany

YOUSUF SOLIMAN, Caltech, USA

MARCEL PADILLA, TU Berlin, Germany

FELIX KNÖPPEL, TU Berlin, Germany

ULRICH PINKALL, TU Berlin, Germany

PETER SCHRÖDER, Caltech, USA

We consider motion effected by shape change. Such motions are ubiquitous in nature and the human made environment, ranging from single cells to platform divers and jellyfish. The shapes may be immersed in various media ranging from the very viscous to air and nearly inviscid fluids. In the absence of external forces these settings are characterized by constant momentum. We exploit this in an algorithm which takes a sequence of changing shapes, say, as modeled by an animator, as input and produces corresponding motion in world coordinates. Our method is based on the geometry of shape change and an appropriate variational principle. The corresponding Euler-Lagrange equations are first order ODEs in the unknown rotations and translations and the resulting time stepping algorithm applies to all these settings without modification as we demonstrate with a broad set of examples.

CCS Concepts: • **Applied computing** → *Physics*; Computer-aided design; • **Computing methodologies** → *Physical simulation; Motion processing*.

Additional Key Words and Phrases: Locomotion, shape space, physical modeling, minimal dissipation, least action, Kirchhoff tensor

## ACM Reference Format:

Oliver Gross, Yousuf Soliman, Marcel Padilla, Felix Knöppel, Ulrich Pinkall, and Peter Schröder. 2023. Motion from Shape Change. *ACM Trans. Graph.* 42, 4, Article 1 (August 2023), 11 pages. <https://doi.org/10.1145/3592417>

## 1 INTRODUCTION

What do cells, spermatozoa, snakes, stingrays, falling cats, astronauts, and platform divers have in common? They all effect motion—rotation and/or translation—through shape change and the resulting motion can be derived from the change of geometry with the aid of a variational principle. Remarkably, the resulting equations are first order in time rather than the usual second order equations of Newtonian dynamics. An algorithm that treats all of the above mentioned settings uniformly for purposes of animation is the subject of this paper.

To introduce the basic outline of our approach we begin with a simple representative example.

### 1.1 A First Example

Consider the motion of a snake. Changing its body shape in a sinusoidal fashion, forward “slithering” motion results. How can we

Authors' addresses: Oliver Gross, TU Berlin, Berlin, Germany, ogross@math.tu-berlin.de; Yousuf Soliman, Caltech, Pasadena, CA, USA, ysoliman@caltech.edu; Marcel Padilla, TU Berlin, Berlin, Germany, padilla@math.tu-berlin.de; Felix Knöppel, TU Berlin, Berlin, Germany, knoeppe@math.tu-berlin.de; Ulrich Pinkall, TU Berlin, Berlin, Germany, pinkall@math.tu-berlin.de; Peter Schröder, Caltech, Pasadena, CA, USA, ps@caltech.edu.

2023. 0730-0301/2023/8-ART1 \$15.00  
<https://doi.org/10.1145/3592417>



Fig. 1. Left: underwater video capture of a sting ray. Right: output of our algorithm based on providing only an undulating surface in the shape of a sting ray. Video 0:04.

model this? Let the instantaneous shape of the snake be given by a univariate curve

$$s \mapsto \gamma(s) \in \mathbb{R}^3 \quad s \in [0, S]$$

and denote the set of all such curves by  $\mathcal{M}$ . This infinite dimensional manifold is invariant under the action of  $G = \text{SE}(3)$ , the group of rigid motions: if  $\gamma \in \mathcal{M}$  then so is  $g(\gamma)$  for  $g \in G$ . We formalize the notion of a shape as the *orbit*

$$G(\hat{\gamma}) = \{g(\hat{\gamma}) \mid g \in G\}$$

representing a single shape in all its possible placements.  $\mathcal{M}$  is the union of all these orbits, which are 6-dimensional submanifolds of  $\mathcal{M}$ . A time indexed family of shapes—deformations of the snake body—then is a map into the set of orbits

$$t \mapsto G(\hat{\gamma}_t) \quad t \in [0, T].$$

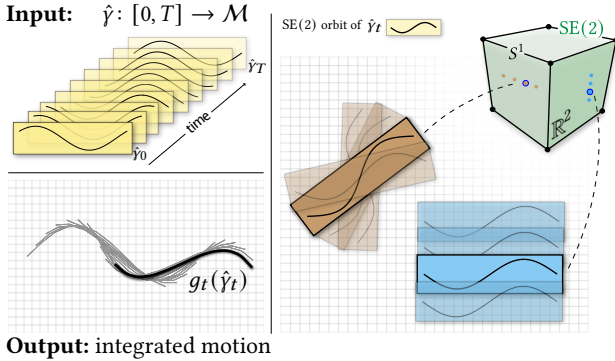


Fig. 2. Our algorithm takes as input a discrete time indexed sequence of shapes. In the case of planar curves the placement and orientation are parameterized by rotations ( $S^1$ ) and translations ( $\mathbb{R}^2$ ) as indicated on the right. Our algorithm then outputs placements and orientations in world space for each shape, realizing the associated motion.

Given such a sequence of shapes we want to find representatives  $\gamma_t \in G(\hat{\gamma}_t)$ —particular placements in world space—realizing the motion induced by shape change (see Fig. 2).

Snake motion is dominated by friction forces which we model with Rayleigh dissipation as proportional to velocity [Strutt, M. A. (Lord Rayleigh) 1871]. Helmholtz' principle of least dissipation [1882] then calls for minimizing the total energy dissipation given by the quadratic form

$$\mathcal{E}(\gamma) = \frac{1}{2} \int_0^T \langle \gamma', \gamma' \rangle_{\mathcal{D}} dt,$$

where  $\gamma'$  denotes the time derivative and  $\langle \cdot, \cdot \rangle_{\mathcal{D}}$  the dissipation metric. Because the shapes  $G(\hat{\gamma}_t)$  are given, we may only vary  $g$  as we go from one orbit to the (infinitesimally) next orbit. To minimize dissipation our movement should therefore be orthogonal—with respect to the dissipation metric—to the orbits: any additional movement in the orbit direction unnecessarily increases dissipation. Importantly, this condition—orthogonality of  $\gamma'$  to the orbits—does not involve  $\gamma''$ . In the absence of external forces we therefore only need to integrate a first order ODE in  $g$  to determine the global motion induced by the shape change.

This reduction of the physical model to a first order 6-dimensional system thanks to the geometry—moving orthogonally to the orbits—applies verbatim to other settings which are dissipation dominated. Remarkably this geometric argument also applies to examples such as the astronaut turning in zero gravity for which only inertial forces matter. In that setting Euler's principle of least action [1744, Addend. II; p. 309] applies and shape change induces motion in accordance with the constancy of momentum.

All these different scenarios are unified when viewed from the perspective of Newtonian mechanics in Riemannian manifolds [Padilla et al. 2019, Eq. 2]. Given a manifold  $\mathcal{M}$  of system states—the shapes of the snake—two Riemannian metrics are at play: the inertia metric which measures the kinetic energy  $\frac{1}{2} \langle \gamma', \gamma' \rangle_{\mathcal{K}}$  and the dissipation metric which measures the energy dissipation due to friction  $\frac{1}{2} \langle \gamma', \gamma' \rangle_{\mathcal{D}}$ . In many interesting settings one of the two metrics dominates, leading to a first order differential equation for the resulting

motion. (For completeness we will also show some second order scenarios which involve both inertial and dissipative effects.)

After briefly reviewing relevant literature we will turn to the general setting and describe our setup in detail. This will be followed by a series of examples and comparisons with acquired sequences to demonstrate the efficacy of our approach.

## 1.2 Related Work

Limbless locomotion such as that of snakes has long fascinated biologists and physicists alike. Early models of snakes and worms were based on the bending of an elastic bar subject to a normal/tangential frictional anisotropy [Kuznetsov et al. 1967] and such models continue to be refined [Hu et al. 2009]. Snakes have also inspired robotic designs [Liljeback et al. 2012] which require physical models for actuation of shape change [Ostrowski and Burdick 1998]. In the computer graphics literature we find mass-spring systems [Miller 1988] and point-based physics [Waszak 2018] simulations controlling the body shape through forces. In contrast, we assume that the shape change is given on input and the only task remaining is the placement of the changing shape in the world coordinate system. In the absence of external forces this requires only the solution of a first order system. In App. A we prove Thm. 2 which is a variant of Noether's theorem [1918] stating that symmetries of variational problems lead to conservation laws. In our case there are as many symmetries as there are effective degrees of freedom and the constancy of the constants of the motion—a first order equation—is equivalent to the original—second order—Euler-Lagrange equations.

More broadly, dissipative models of motion through shape change govern small organisms [Guasto et al. 2020] which “swim” in very low Reynolds number environments [Lauga and Powers 2009; Elgeti et al. 2015]. These are governed by Aristotelian—first order—mechanics [Purcell 1977] with “their motion governed entirely by the sequence of shapes the swimmer assumes.” [Shapere and Wilczek 1989a]. Relevant for our purposes is that shape change is everything in the dissipative limit regime, and—as we will show—continues to work remarkably well outside the limiting regime and with very simple dissipation models.

A formally identical—first order—treatment is possible for settings without dissipation but with constant, not necessarily zero, linear and angular momentum. An example is the astronaut who uses shape change to reorient with zero angular momentum [Kulwicki and Schlei 1962]. Similarly, the falling cat rights herself without

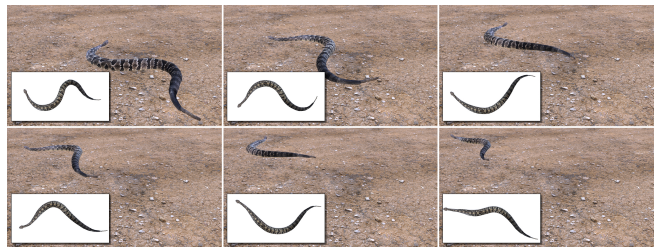


Fig. 3. Starting with an animator provided sequence of snake shapes in model local coordinates [Daye 2019] the placement in the global frame is produced as the output of our simulation. Video 1:10.

any angular momentum [Kane and Scher 1969; Montgomery 1993], an observation that has long intrigued researchers [Marey 1894]. Relatedly, the platform diver—who manages complex sequences of twists and somersaults—does so with constant, non-zero angular momentum [Frohlich 1979, 1980]. Wooten and Hodges [1996] demonstrated second order Newtonian physics simulations of platform divers, using force based controllers to effect the required shape changes.

Motion due to shape change also appears in ideal fluids [Kuznetsov et al. 1967; Kozlov and Ramodanov 2001] and not just in the dissipative limit regime. The only difference here is that the inertia tensor has to account for the inertia of the body as well as that of the surrounding fluid [Kirchhoff 1870, 1876]. This can be accomplished by solving a boundary value problem [Kanso et al. 2005; Weissmann and Pinkall 2012], avoiding the need to simulate the fluid over the entire volume [Tan et al. 2011; Lentine et al. 2011]. Further efficiencies can be gained by modeling the effect of the fluid through local thrust and drag models [Tu and Terzopoulos 1994; Wu and Popović 2003; Ju et al. 2013; Min et al. 2019], as we do.

### 1.3 Contributions

We give a unified algorithm for motion arising from shape changes. It applies to curves as much as to surfaces, as well as more general settings, with no significant modifications. Suitable scenarios that can be modeled in this way include motion in various types of media. In each case the motion minimizes a variational energy. In the absence of external forces, the resulting equations are first order in the Euclidean motion placing the shape sequence in the world coordinate frame. We demonstrate the efficacy of our approach with a broad range of motion scenarios.

## 2 DYNAMICS OF SHAPE CHANGE

We are interested in understanding how motion can be effected by shape change. Thus we consider the changing shape—typically animator designed—as *input* to our algorithm, leaving us with only 6 degrees of freedom—rotation and translation into the world coordinate system—to be determined at each time. We address three principal, idealized settings, which will be handled by our uniform approach and algorithm. Sec. 2.1 considers dissipation dominated motion using the dissipation metric; Sec. 2.2 considers motion in a negligible medium using the standard inertia metric; and Sec. 2.2.1 considers motion in an inviscid fluid using the extended inertia (Kirchhoff) metric.

The common setup deals directly with space discrete objects. Hence a *positioned shape* is a collection of vertices with point positions

$$\gamma = \{p_j \in \mathbb{R}^3 \mid j \in (1, \dots, n)\} \in (\mathbb{R}^3)^n$$

in general position. The totality of such positioned shapes will be denoted  $\mathcal{M}$ . Typical examples of  $\mathcal{M}$  are the vertex positions of polylines approximating curves and of triangle meshes approximating surfaces, though more general arrangements of points, for example, skeleton rigs, also appear. When a positioned shape is transformed by a rigid motion  $g \in G := \text{SE}(3)$  it is understood that any vectors at the vertices are transformed as well although using only the rotation

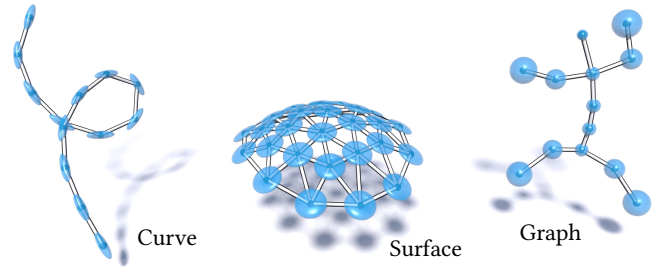


Fig. 4. Visualization of the metric tensors  $B_j^Y$  as ellipsoids at the vertices of curves (tangentially oriented), surfaces (normally oriented), and more general graphs (here: rig skeletons with point masses). The long principal axes of the ellipsoids indicate directions in which motion is relatively easier.

part of  $g$ . A *shape*

$$G(\dot{\gamma}) := \{g(\dot{\gamma}) \mid g \in G\}$$

is the set of all possible placements of  $\dot{\gamma}$ . To describe the different metrics, let  $B^Y \in \mathbb{R}^{3n \times 3n}$  be a positive definite, self-adjoint operator (typically dependent on  $\gamma$ ). For  $\dot{\gamma}, \ddot{\gamma} \in T_\gamma \mathcal{M}$  two tangent vectors at  $\gamma \in \mathcal{M}$  the associated metric is given by

$$\langle \dot{\gamma}, \ddot{\gamma} \rangle_{\mathcal{B}} = \langle B^Y \dot{\gamma}, \ddot{\gamma} \rangle$$

where  $\langle \cdot, \cdot \rangle$  is the standard Euclidean metric. Additionally we require the resulting metric to be invariant under rigid motions

$$\langle \dot{\gamma}, \ddot{\gamma} \rangle_{\mathcal{B}} = \langle g(\dot{\gamma}), g(\ddot{\gamma}) \rangle_{\mathcal{B}} \quad g \in G.$$

In our examples the metric tensors are taken to be block diagonal with blocks at each vertex of the form

$$B_j^Y := \alpha_j I + \beta_j P_j \quad (1)$$

where  $\alpha_j, \beta_j \in \mathbb{R}$  are arbitrary constants,  $I$  the identity on  $\mathbb{R}^3$ , and  $P_j$  the projector onto the normal space at  $j$ . For curves, with unit tangent vectors  $t_j$ ,  $P_j := I - t_j \otimes t_j$ . For surfaces with unit normal vector  $n_j$ ,  $P_j := n_j \otimes n_j$ . As integrated quantities, the weights  $(\alpha_j, \beta_j)$  should include an integration factor  $m_j$  representing lumped mass proportional to length, area, or volume according to the underlying domain of integration (Table 1). Fig. 4 visualizes typical  $B_j^Y$  for different settings. The physical meaning of  $(\alpha_j, \beta_j)$ , and how to set them, is discussed in Secs. 2.1, 2.2, and 2.2.1.

Suppose now we are given a (continuous) time indexed family of shapes over some time interval

$$[0, T] \ni t \mapsto \hat{\gamma}_t \in \mathcal{M}$$

prescribing a sequence of deforming shapes. Our task then is to find Euclidean motions  $g_t \in G$  to place the shapes into world space:

$$\gamma_t = g_t(\hat{\gamma}_t).$$

Note that since  $\hat{\gamma}_t$  is given on input the only variable we get to control—and must determine—is  $g_t$ .

We now turn to the particulars of motion in different media. They are distinguished by the choice of parameters and the physical meaning of the metric tensors  $B_j^Y$  as well as the use of an appropriate variational principle for the determination of  $g_t$ .

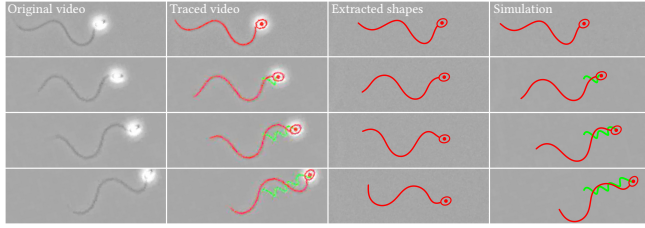


Fig. 5. Swimming sperm present an example of the dissipative limit with very high viscosity. First column: acquired video of sperm motion [Guasto et al. 2020]; second column: movement trace of the “head” in green; third column: shapes given as input to our algorithm; fourth column: result of our simulation ( $m_{\text{head}} = 3m_j$ ). Video 0:36.

## 2.1 Dissipation-Dominated Motion

For tiny creatures (like bacteria) water appears to be highly viscous and the surrounding fluid moves according to the equations of Stokes flow [Rieutord 2015, Ch. 4]. This means that the fluid velocity minimizes dissipation among all divergence-free vector fields compatible with a no-slip condition on the boundary of the shape-changing body. In this limit friction forces are truly linear in the velocities of the points on the body boundary, so our assumption of Rayleigh dissipation is strictly valid. For larger creatures like stingrays (Fig. 1) or jellyfish (Fig. 8), i.e., at higher Reynolds numbers, drag forces depend on velocities in a non-linear fashion and a variety of mechanisms (like vortex shedding) contribute to drag [Vogel 1983, Ch. 5] (see also [Ju et al. 2013; Min et al. 2019]). No less, we obtain surprisingly realistic results if we continue to use Rayleigh dissipation as our drag model.

To model these settings,  $\langle \cdot, \cdot \rangle_B$  is chosen to be the *dissipation metric* on  $\mathcal{M}$ . The associated quadratic form  $\frac{1}{2}|\gamma'|_{\mathcal{D}}^2$  captures the *energy dissipation*. The total energy dissipation of a path  $[0, T] \ni t \mapsto \gamma_t \in \mathcal{M}$  is given by

$$\mathcal{E}(\gamma) = \frac{1}{2} \int_0^T |\gamma'_t|_{\mathcal{D}}^2 dt. \quad (2)$$

In order to determine the family  $t \mapsto g_t$  we appeal to Helmholtz’ principle of least dissipation [1882]. With  $\gamma_t$  constrained to be an element of the prescribed orbit  $G(\hat{\gamma}_t)$ —and given an initial placement  $\gamma_{t=0} = \hat{\gamma}_0$ —Helmholtz’ principle tells us that the actual positioning  $t \mapsto \gamma_t$  due to shape change is the one that minimizes  $\mathcal{E}(\gamma)$  under all variations compatible with the constraints

$$\gamma_{t=0} = \hat{\gamma}_0 \quad \gamma_t \in G(\hat{\gamma}_t) \quad \forall t \in [0, T].$$

This leads to the following geometric characterization:

**THEOREM 1.** *A curve  $\gamma: [0, T] \rightarrow \mathcal{M}$  solves the equation of motion for movement in a highly viscous medium if and only if  $\gamma$  is orthogonal to the orbits, i.e., if*

$$\gamma'_t \perp T_{\gamma_t} G(\hat{\gamma}_t) \quad \forall t \in [0, T].$$

**PROOF.** A consequence from Thm. 2 for zero momentum.  $\square$

In App. A, where we describe the differential geometry underlying our dynamical model, the component of  $\gamma'$  tangent to the orbits determines the momentum. Thm. 1 says that for a shape-changing body whose motion is dissipation dominated this momentum vanishes.

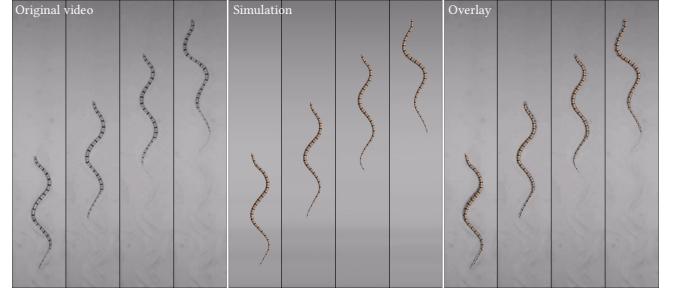


Fig. 6. Left: video capture of a snake [Schiebel et al. 2019]; middle: result of our simulation; right: overlay of captured and simulated data. Video 0:55.

Our setup for modeling dissipation applies verbatim to settings with a highly viscous medium (Fig. 5). It is however also effective in settings such as slithering locomotion of snakes. Fig. 6 shows a comparison of shape data from video capture and the output of our algorithm, showing excellent agreement for this simple motion. Fig. 17 shows an example of more complex motion capture. In other settings (Fig. 3) the changing shape is modeled by an animator in a local coordinate frame and then moved to the global frame by our algorithm. In all of these settings the dissipation tensor was parameterized by a single *anisotropy* parameter  $\epsilon \in [0, 1]$ , setting  $(\alpha_j, \beta_j) = m_j(\epsilon, 1 - \epsilon)$  (Table 1). This anisotropy parameter  $\epsilon$  controls the ease of tangential motion compared to normal motion  $\alpha_j / (\alpha_j + \beta_j) = \epsilon$ . For “swimmers” in Stokes flow  $\epsilon = 1/2$  is a typical value [Lauga and Powers 2009, Sec. 4.3]. In fact, drag based thrust is not possible unless such a tangential/normal anisotropy in viscous dissipation is present [Gray and Hancock 1955]. In the case of snakes,  $\epsilon$  captures well motion on different substrates (Fig. 7: from gravel  $\epsilon \approx 0$  to velvet  $\epsilon \approx 1$ ).

What happens with motion at higher Reynolds number (lower viscosity)? In that case energy dissipation is due to two sources. The first is motion of the body normal to its surface. This sets the whole fluid in motion and thereby transfers energy to the fluid, for example in the form of vortex shedding. This pathway of energy dissipation is not directly dependent on the fluid viscosity and its

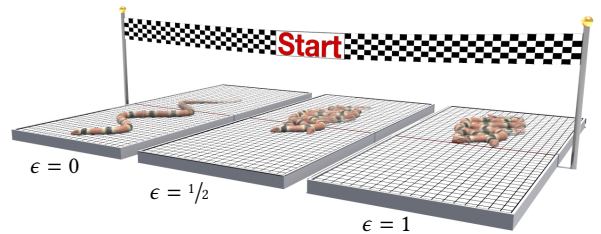


Fig. 7. A dissipation anisotropy is required for forward motion [Gray and Hancock 1955]. The ratio of tangential/normal anisotropy controls the effectiveness of forward motion.  $\epsilon$ . Video 3:20.

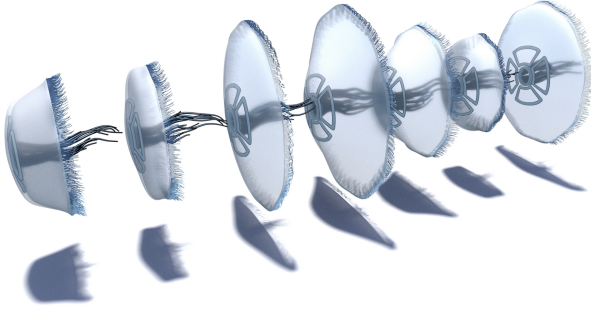


Fig. 8. Computed by our algorithm: the motion of a stylized jellyfish swimming in an high Reynolds number fluid solely by the animator designed cyclic motion of its umbrella. Video 0:20.

local contribution is captured by  $\alpha_j + \beta_j$ . The second pathway arises from viscous friction in a thin boundary layer around the moving body. The energy dissipated in this way is proportional to surface area, the squared norm of the tangential component of velocity, and the fluid viscosity. The local contribution of this part of energy dissipation is captured by  $\alpha_j$ . In the literature [Vogel 1983, Ch. 5] and [Ju et al. 2013; Min et al. 2019] the isotropic part of the local dissipation tensor ( $\alpha_j$ ) is called *drag* while the normal part ( $\alpha_j + \beta_j$ ) is referred to as *thrust*. In our high Reynolds number examples Figs. 1 and 8, we found viscosity negligible, corresponding to  $\epsilon \approx 0$ .

So far we have treated motion which is dissipation dominated. In that setting the dynamic momentum vanishes (Thm. 1). In the next subsection we will encounter a physical scenario where there can be non-zero momentum.

## 2.2 Inertia-Dominated Motion

Suppose that the shape-changing body of Sec. 2.1 is no longer immersed in a dissipation dominated environment but rather in a medium such as air or a vacuum, whose influence on the motion we can safely neglect. Then the relevant physical principle is no longer Helmholtz' principle of least dissipation but Euler's principle of least action. This implies two changes:

- The relevant Riemannian metric on  $\mathcal{M}$  now defines the kinetic energy  $\frac{1}{2}|\gamma'|_{\mathcal{K}}^2$  instead of the energy dissipation due to viscous friction.
- The admissible variations of  $\gamma: [0, T] \rightarrow \mathcal{M}$  are limited to those fixing both end points  $\gamma_0$  and  $\gamma_T$ .

In either case the equations of motion arise from minimizing the quadratic form defined by the respective metric and are formally identical. This implies that we can use a single algorithm for settings which are either dissipation or inertia dominated.

To see this note that if the points  $p_j \in \gamma$  carry mass  $m_j$  the corresponding inertia tensor, which gives us the kinetic energy, is given by  $(\alpha_j = m_j, \beta_j = 0)$  (Eq. (1)). Given  $\gamma \in \mathcal{M}$  moving with velocity  $\gamma'$ , *angular momentum*  $\mathbf{l}$  and *linear momentum*  $\mathbf{p}$  of  $\gamma$  are given by

$$\mathbf{l} := \sum_{j=1}^n m_j p_j \times p'_j \quad \mathbf{p} := \sum_{j=1}^n m_j p'_j. \quad (3)$$

Suppose now we are dealing with a shape-changing body that is not subject to any external forces—such as gravity or forces from the surrounding medium. Then the arguments in App. A show that a curve  $\gamma: [0, T] \rightarrow \mathcal{M}$ —subject to the constraints  $\gamma_t \in G(\dot{\gamma}_t)$ —satisfies *Euler's principle of least action* [1744, Addend. II; p. 309] if and only if angular and linear momentum are both constant in time—though they need not be zero.

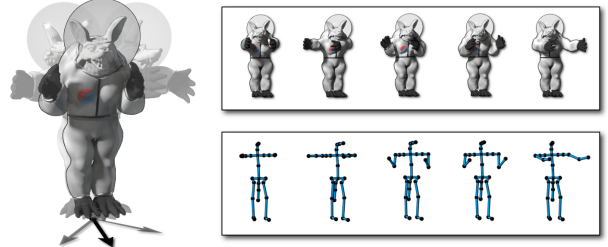


Fig. 9. The shape change of the Armadillo astronaut is controlled by a skeleton rig with point masses at the joints. Using this sequence of shapes as input to our algorithm the astronaut manages to turn 90° over several cycles while angular momentum remains zero throughout. Video 1:21.

For example, Fig. 9 shows an astronaut initially at rest and hence with zero linear and angular momentum at all times. Yet, through a sequence of shape changes, the astronaut is able to rotate [Kulwicki and Schlei 1962].

When the only external forces come from gravity, we essentially are still in a zero gravity situation: The center of mass of a shape-changing body follows a parabola, while in a coordinate system that

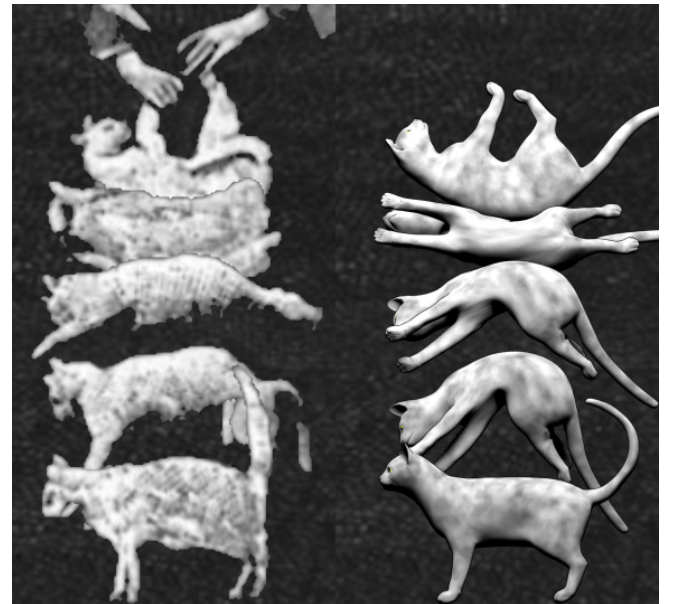


Fig. 10. Left: photographic capture of the cat righting reflex [Marey 1894] with zero angular momentum. Right: output of our algorithm after controlling the cat shape through a skeleton rig with point masses. Vertical motion of the center of mass due to gravity was added separately. Video 1:47.

translates with the center of mass we see a zero gravity motion with zero linear momentum. For the falling cat [Marey 1894] (Fig. 10) the angular momentum is zero, so it is in a similar situation as the astronauts [Shapere and Wilczek 1989b]. Similarly, platform divers (Fig. 11) carry constant though non-zero angular and linear momentum—ignoring gravity—after pushing off the platform and yet master intricate sequences of twists and somersaults through carefully sequenced shape changes [Frohlich 1979, 1980; Wooten and Hodges 1996].

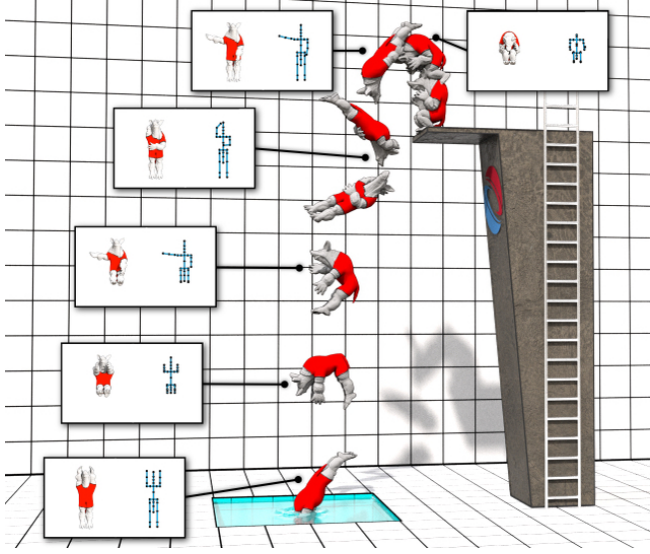


Fig. 11. Platform diver executing a twist and somersault sequence controlled by their shape change which in turn was controlled by a skeleton rig with point masses. Motion of the center of mass due to gravity was added separately. The jump represents a case of constant but non-zero angular and linear momentum. Video 2:18.

In all the inertia dominated settings we have considered so far the medium played no role. Consequently we were able to account for the effect of gravity a posteriori, keeping the constant momentum setting. This changes when the medium has significant inertia itself, a case to which we now turn.

**2.2.1 Motion in Inviscid Fluid.** The motion of a shape-changing body in an inviscid fluid, *i.e.*, without viscous losses, continues to be governed by Euler’s principle of least action. But this time with regard to the kinetic energy  $\frac{1}{2}|\gamma'|_{\mathcal{K}}^2$  held by the *combined* body and fluid system. To avoid simulating the fluid volume [Tan et al. 2011; Lentine et al. 2011] we need an estimate of the kinetic energy of the fluid. The most conservative such estimate is given by the unique gradient flow compatible with the motion of the shape-changing body [Da et al. 2016; Padilla et al. 2019]. This Neumann boundary value problem, while avoiding simulating the fluid volume, still requires a global solve over the bounding surface [Kanso et al. 2005]. In the context of rigid bodies under water—no shape change—this idea was first developed by Gustav Kirchhoff [1870; 1876] and later applied to shape-changing bodies [Kuznetsov et al. 1967; Kozlov and Ramodanov 2001; Kanso et al. 2005]. Here we see that such an

approach to swimming in water fits the computational framework we have built so far. Since the Kirchhoff Ansatz uses no-through boundary conditions, we can view the second summand in the inertia metric tensor

$$K_j^\gamma = \alpha_j I + \beta_j P_j$$

as an approximation of the contribution of the motion of boundary vertex  $j$  to the kinetic energy of the fluid [Tu and Terzopoulos 1994].

**2.2.2 Summary.** All the settings we have seen so far are characterized by being either inertia or dissipation dominated with constant, though not necessarily zero, angular and linear momentum. Some settings though require accounting for both inertial and dissipative effects: The rock sinking in water would forever accelerate were it not for dissipation or penetrate the sea floor unless collision forces stop it. More generally we may want to apply other external forces. Any such scenarios are easily accommodated by extending our basic method. Instead of integrating an equation constrained by the constancy of momentum along the motion path, we now have momentum varying according to the applied forces, be they dissipative, collision induced, or otherwise (Secs. 3.1.1, and 3.1.2).

### 3 TIME DISCRETIZATION

We now turn our attention to time discretization. Starting with a discrete time indexed sequence of shapes with  $n$  points each

$$\hat{\gamma}_0, \dots, \hat{\gamma}_T \in \mathcal{M} = (\mathbb{R}^3)^n,$$

our goal is to determine rigid motions  $g_t \in \text{SE}(3)$  that position the shapes ( $\gamma_t := g_t(\hat{\gamma}_t)$ ) according to the physical principles described in the previous section. We discretize the energy as

$$E(\gamma_0, \dots, \gamma_T) := \sum_{t=1}^T E(\gamma_{t-1}, \gamma_t),$$

where the two-point energy  $E(\gamma_{t-1}, \gamma_t)$  discretizes the smooth integrals by averaging the Riemannian metrics at the endpoints and using linear displacements as discrete time derivatives as is standard in variational time integrators [Marsden and West 2001]

$$E(\gamma_{t-1}, \gamma_t) := \left\langle \frac{1}{2}(B^{\gamma_t} + B^{\gamma_{t-1}})\Delta p^t, \Delta p^t \right\rangle \quad \Delta p^t := p^t - p^{t-1}, \quad (4)$$

where  $p^t \in (\mathbb{R}^3)^n$  is the concatenation of all  $n$  point positions of  $\gamma_t$ . One can check that  $E$  is equivariant with respect to the  $\text{SE}(3)$  action

$$E(g(\gamma_{t-1}), g(\gamma_t)) = E(\gamma_{t-1}, \gamma_t) \quad g \in \text{SE}(3).$$

Other discretizations of the energy per time edge can be used, provided they respect this  $\text{SE}(3)$  symmetry.

In App. C we compute the Euler-Lagrange equations of the discretized energy, which determine constants of motion  $\mu_t \in \mathbb{R}^6$  that we call *momenta* of the changing shape

$$\mu_t := \begin{pmatrix} -\sum_j p_j^t \times (B^{\gamma_{t-1}} \Delta p^t)_j + p_j^{t-1} \times (B^{\gamma_t} \Delta p^t)_j \\ -\sum_j ((B^{\gamma_t} + B^{\gamma_{t-1}}) \Delta p^t)_j \end{pmatrix}. \quad (5)$$

#### 3.1 Time Integration

The unknown motion is uniquely determined by the constancy of the momenta. Discrete time integration proceeds through iterative placement of shapes preserving the momentum on each time edge  $[t-1, t]$  (Cor. 1 in App. B) as implemented in Algs. 1 and 2. For the

non-linear solver needed in Alg. 2 we use SciPy’s Newton method with a Krylov approximation of the inverse Jacobian.

---

**Algorithm 1 – DiscreteMomenta( $\gamma, \tilde{\gamma}$ )**


---

**Input:** consecutive shapes ( $\gamma, \tilde{\gamma}$ )

**Output:**  $\mathbb{R}^6$ -momenta  $\mu$

- 1: compute tensors  $B^Y, B^{\tilde{Y}}$
  - 2: compute displacements  $\Delta\tilde{p} \leftarrow \tilde{p} - p$
  - 3:  $\mu^1 \leftarrow -\sum_j \tilde{p}_j \times (B^Y \Delta\tilde{p})_j + p_j \times (B^{\tilde{Y}} \Delta\tilde{p})_j$
  - 4:  $\mu^2 \leftarrow -\sum_j ((B^Y + B^{\tilde{Y}}) \Delta\tilde{p})_j$
  - 5:  $\mu \leftarrow (\mu^1 \ \mu^2)^\top$
- 

---

**Algorithm 2 – IntegrateMotion( $\mu_0, \hat{\gamma}_0, \dots, \hat{\gamma}_T$ )**


---

**Input:** shapes and target momentum ( $\mu_0, \hat{\gamma}_0, \dots, \hat{\gamma}_T$ )

**Output:** positioned shapes  $\gamma_0, \dots, \gamma_T$

- 1:  $\gamma_0 \leftarrow \hat{\gamma}_0$
  - 2: **for**  $t = 1, \dots, T$  **do**
  - 3:    $g_t \leftarrow \text{solve DiscreteMomenta}(\gamma_{t-1}, g_t(\hat{\gamma}_t)) = \mu_0$
  - 4:    $\gamma_t \leftarrow g_t(\hat{\gamma}_t)$
  - 5: **end for**
- 

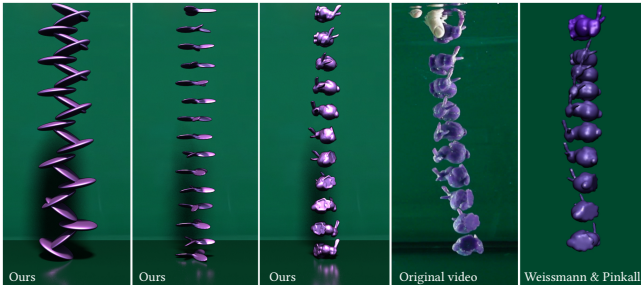


Fig. 12. Rigid bodies falling underwater with terminal velocity, resulting from a balance between dissipative and gravitational forces (see Sec. 3.1.1). Compare to actual video capture and the ever accelerating simulation without dissipation from [Weißmann and Pinkall 2012]. Video 3:07.

**3.1.1 Underwater Dynamics.** In Fig. 12 we demonstrate a variety of (rigid) bodies falling underwater with terminal velocity, which is characterized by the balance between gravitational and dissipative forces. This setting can still be accommodated by our first order integration method. Specifically, we use a dissipation metric  $D^Y$  for Eq. (5) and modify the right-hand side in Step 3 of Alg. 2 to account for the gravitational force and torque by setting

$$\mu_t \leftarrow \Delta t \varrho_{t-1}, \quad \varrho_t = \left( \frac{\sum_j m_j p_j^t \times g}{\sum_j m_j g} \right) \quad (6)$$

for  $g$  the gravitational acceleration vector. This setting also admits a simple treatment of collision with the floor where penetration is prevented by a reaction force of contact (Fig. 12). More generally though one may need to go to a second order dynamics setting.

**3.1.2 Transition to Second Order.** As an example of a second order treatment consider external forces such as gravity or dissipation acting in an inertial setting. One way to accommodate the now changing momentum with minimal modification of our integration scheme is to use the semi-implicit Euler scheme for second order problems [Hairer and Wanner 2015]. In a first step the momentum is explicitly updated by letting the force  $\varrho_t$  act for the duration of the time step. Then we solve for the new position as a function of the updated momentum in a second step, i.e., Step 3 in Alg. 2 becomes

$$\begin{aligned} \mu_t &\leftarrow \mu_{t-1} + \Delta t \varrho_{t-1} \\ g_t &\leftarrow \text{solve DiscreteMomenta}(\gamma_{t-1}, g_t(\hat{\gamma}_t)) = \mu_t. \end{aligned}$$

Specifically, for the force of gravity,  $\varrho_t$  is chosen according to Eq. (6) while for dissipation forces (Figs. 13 and 16),  $\varrho_t$  is chosen as  $\mu_t$  from Eq. (5) with a dissipation metric ( $B^Y$  set to  $D^Y$ ).

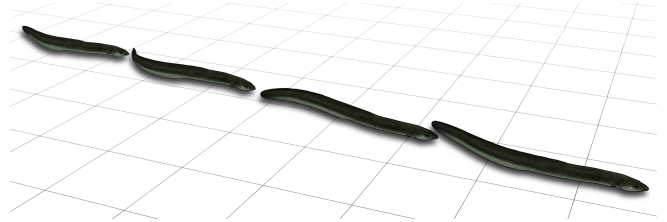


Fig. 13. An Eel swimming modeled by second order dynamics (Sec. 3.1.2) in an inertia dominated environment subject to dissipation forces. Video 2:56.

## 4 DISCUSSION

We have implemented our algorithm in SideFX’ Houdini and used it for all simulations and visualizations shown. The full code is available in the supplementary material. We use this section to discuss our experiments which are also documented in the accompanying video.

### 4.1 Validation and Results

To validate the accuracy of our discrete time integration we consider two scenarios: *Purcell’s Scallop Theorem* and the *Dzhanibekov effect*. Purcell’s scallop theorem states that a cyclic shape change controlled by a single degree of freedom cannot produce net motion in high viscosity media [Purcell 1977]. Our time integration reproduces this theorem up to the accuracy of our solver (Fig. 16 inset). The Dzhanibekov effect, due to the intermediate axis theorem, states that rotation around the intermediate inertial axis is unstable and leads to periodic orientation changes while angular momentum remains constant [Landau and Lifshitz 1976, p. 118]. Fig. 14 shows a half cycle of this phenomenon and our integrator faithfully reproduces it to within the accuracy of the solver.

To see how well our model for viscous media performs we have run a number of comparisons with acquired data. Fig. 5 shows video capture of spermatozoön motion. With the extracted shapes our algorithm faithfully reproduces the initially observed motion. This demonstrates that our model of viscous losses matches swimming in very low Reynolds number fluid media well. Fig. 6 uses the same model even though it is not strictly applicable. No less it works well for simple snake motion. Fig. 3 shows an example of putting our method to work for animator modeled shape changes.



Fig. 14. Rotation about the intermediate inertial axis is unstable [Poincaré 1851] (see also [Landau and Lifshitz 1976, p. 118]), leading to periodic orientation changes. Our algorithm keeps angular momentum constant by construction which allows us to faithfully reproduce such instability phenomena. Here a single (half) cycle is shown with the intermediate axis marked as it traces out a 180° turn. Video 3:40.

Using acquired underwater video of a stingray as a reference, we modeled its motion in a low-dissipation (high Reynolds number) environment (Fig. 1). Steering of our simulated stingray is summarized in Fig. 15. Similarly, the jellyfish (Fig. 8) moves in a low-dissipation environment by its cyclic umbrella motion alone.

For settings involving a negligible medium we demonstrated the orientation change of the astronaut through suitable arm motions (Fig. 9). Another example of this type is the falling cat (Fig. 10)—which we compare with the historic photographs of Marey [1894]—and the platform diver (Fig. 11). For these examples we used simple skeleton rigs animated through keyframing.

In some settings both inertial and dissipative effects are important. Fig. 12 shows underwater motion at terminal velocity due to the balance of gravitational and dissipative forces. This setting can still be accommodated by our first order method (Sec. 3.1.1). More generally though inclusion of external forces in an inertial setting requires second order dynamics and an associated integrator (Sec. 3.1.2). As a simple demonstration we consider the motion of an eel (Fig. 13). In between cyclical “strokes” the eel briefly stops changing its shape. In a purely dissipative setup—such as what we used for the snakes—this leads to a break in the forward motion. If instead we are in an inertial setting with dissipation modeled as an external force the eel “glides” during these breaks in the shape change, a more realistic result.

#### 4.2 Performance

The examples we presented were computed in near real time when run on an Apple M1 Max CPU. Table 1 provides an overview of

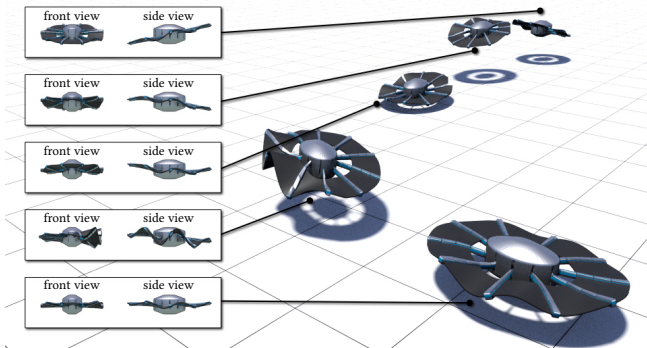


Fig. 15. Underwater robot moving based on the same principle as the stingray (see Fig. 1), indicating how it can be steered up/down as well as left/right. Video 4:09.

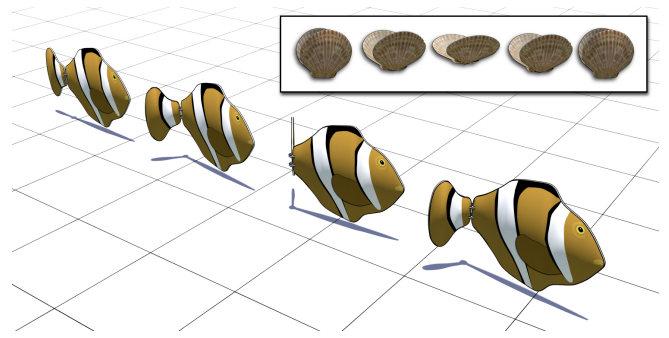


Fig. 16. According to Purcell’s scallop theorem [1977] single degree of freedom shape change in a highly viscous medium yields no net motion (inset). If inertia is accounted for, motion is possible. Video 3:31.

typical computation times and curve/mesh/graph resolutions. The performance is seemingly unaffected by the number of vertices of the input geometries, but rather depends on the difficulty of the root-finding problem (Sec. 3).

Table 1. Parameters and computation times of our algorithm (Sec. 3).

Fig.	Data	Vertices	$m_j$	$\epsilon$	avg. Timesteps per Second
1	surface	891	Area( $j$ )	1/4	13
8	surface	612	Area( $j$ )	1/10	19
5	curve	36	Length( $j$ )	1/2	10
6	curve	23	Length( $j$ )	1/20	141
3	curve	36	Length( $j$ )	1/20	64
9	graph	30	1	1	124
10	graph	37	1, ( $m_{\text{legs}} = 1/5$ )	1	149
11	graph	30	1	1	100
13	surface	7100	Area( $j$ )	1	4
12	surface	524	Area( $j$ )	1/5	23
16	surface	190	1	1	85
14	graph	24	1	1	192
15	surface	600	Area( $j$ )	0	26
17	curve	51	Length( $j$ )	2/5	41

#### 4.3 Limitations and Possible Refinements

For a shape-changing body in a medium with negligible inertia such as air our basic algorithm is fairly complete and can include gravity *a posteriori*. Similarly complete is the treatment of shape-changing bodies in dissipation dominated environments, where any external force and torque would directly appear as a right-hand side in the equation that we solve in each time step (Sec. 3.1.1).

More general external forces though would need to be accounted for by adding the currently acting torque and force to the—no longer constant—angular and linear momentum (Sec. 3.1.2).

For a swimmer in an ideal fluid we assumed that the flow around the body is irrotational, which excludes phenomena where vortex shedding plays a significant role. In our current approach we treat vorticity production as dissipative loss ignoring any possible effect of the shed vorticity back onto the shape-changing body.

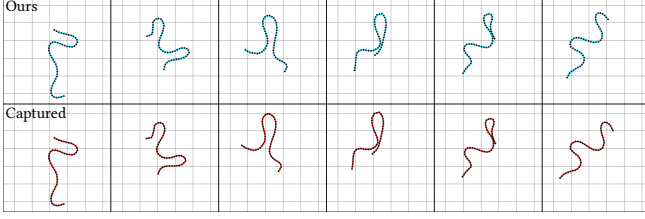


Fig. 17. Motion capture data of a snake moving in complex ways (bottom) [Graphics & Extended Reality Lab 2022] compared with the output of our algorithm (top). Video 4:27.

Other limitations are due to the simplicity of our friction model. Detailed models of snake locomotion account for non-linear friction effects such as directionality of scales [Hu et al. 2009]. These are not captured by viscous dissipation, making it difficult for our method to match complex motion capture data of real snakes with high precision (Fig. 17). On the other hand, it is remarkable how well such coarse approximations can work in settings which are far from the abstract mathematical ideal.

## 5 CONCLUSION AND OUTLOOK

We presented a simple and efficient algorithm for computing motions effected by shape changes. The physical scenarios we considered are distinguished as dissipation dominated or inertia dominated motion. Our mathematical framework provides a unified treatment of these different setups and leads to formally identical equations of motion. Based on the constancy of momenta, the Euler-Lagrange equations are first order ODEs and a standard variational integrator provides for an accurate single step time integration.

So far we have used only very simple metric tensors. It would be interesting to see what other physical scenarios can be modeled by more elaborate tensors. As an example, consider a worm moving by varying the thickness of its body, which can be modeled through time-dependent  $(\alpha_j, \beta_j)$  (Fig. 18).

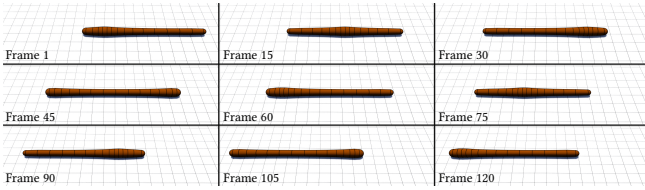


Fig. 18. Changing the weights  $m_j$  according to varying the thickness the earthworm starts crawling. Video 4:48.

Another interesting direction to explore is motion control: how should shape changes be designed to achieve particular motion objectives? Some initial experiments in the direction of steering are depicted in Fig. 15 and used in the production of Fig. 1. We leave exploration of the control problem to future work.

## ACKNOWLEDGMENTS

The bunny and armadillo mesh are used courtesy of the Stanford Computer Graphics Laboratory. We are grateful to Daniel Daye,

Jer Bot, Johnson Martin, Robert Gutierrez, Shahid Abdullah and the TOSCA dataset authors [Bronstein et al. 2008] for making the models of the rattlesnake, eel, clam, and cat available. This work was supported in part by the Deutsche Forschungsgemeinschaft (DFG - German Research Foundation) - Project-ID 195170736 - TRR109 “Discretization in Geometry and Dynamics”, the Caltech Center for Information Science & Technology, and the Einstein Foundation Berlin. Additional support was provided by SideFX software.

## REFERENCES

- Alexander M. Bronstein, Michael M. Bronstein, and Ron Kimmel. 2008. *Numerical Geometry of Non-rigid Shapes*. Springer.
- Fang Da, David Hahn, Christopher Batty, Chris Wojtan, and Eitan Grinspun. 2016. Surface-only Liquids. *ACM Trans. Graph.* 35, 4 (2016), 78:1–12.
- Daniel Daye. 2019. Rigged and Animated Scan of Timber Rattlesnake. <https://sketchfab.com/>. CC Attribution-NonCommercial.
- J. Elgeti, R. G. Winkler, and G. Gompper. 2015. Physics of Microswimmers—Single Particle Motion and Collective Behavior: a Review. *Rep. Prog. Phys.* 78 (2015).
- Leonhard Euler. 1744. *Methodus Inveniendi Lineas Curvas Maximi Minive Proprietate Gaudentes*. Bousquet, Lausanne & Geneva. English translation at WikiSource.
- Cliff Frohlich. 1979. Do Springboard Divers Violate Angular Momentum Conservation? *Amer. J. Phys.* 47, 7 (1979), 583–592.
- Cliff Frohlich. 1980. The Physics of Somersaulting and Twisting. *Sci. Am.* 242, 3 (1980), 154–165.
- Graphics & Extended Reality Lab. 2022. Large Whip Snake. <https://sketchfab.com/>. CC Attribution.
- J. Gray and G. J. Hancock. 1955. The Propulsion of Sea-Urchin Spermatozoa. *J. Exp. Biol.* 32, 4 (1955), 802–814.
- Jeffrey S. Guasto, Jonathan B. Estrada, Filippo Menolascina, Lisa J. Burton, Mohak Patel, Christian Franck, A. E. Hosoi, Richard K. Zimmer, and Roman Stocker. 2020. Flagellar Kinematics Reveals the Role of Environment in Shaping Sperm Motility. *J. Roy. Soc. Interface* 17, 20200525 (2020), 10 pages.
- Ernst Hairer and Gerhard Wanner. 2015. Euler Methods, Explicit, Implicit, Symplectic. In *Encyclopedia of Applied and Computational Mathematics*, Björn Engquist (Ed.). Springer, 451–455.
- David L. Hu, Jasmine Nirody, Terri Scott, and Michael J. Shelley. 2009. The Mechanics of Slithering Locomotion. *Proc. Natl. Acad. Sci.* 106, 25 (2009), 10081–10085.
- E. Ju, J. Won, J. Lee, B. Choi, J. Noh, and M. Gyu Choi. 2013. Data-Driven Control of Flapping Flight. *ACM Trans. Graph.* 32, 5 (2013), 151:1–12.
- T. R. Kanu and M. P. Scher. 1969. A Dynamical Explanation of the Falling Cat Phenomenon. *Int. J. Solids Structures* 5 (1969), 663–670.
- Eva Kanso, Jerrold E. Marsden, Clancy W. Rowley, and J. B. Melli-Huber. 2005. Locomotion of Articulated Bodies in a Perfect Fluid. *J. Non-L. Sci.* 15 (2005), 255–289.
- Gustav Kirchhoff. 1870. Ueber die Bewegung eines Rotationskörpers in einer Flüssigkeit. *J. Reine Angew. Math.* 1870, 71 (1870), 237–262.
- Gustav Kirchhoff. 1876. *Vorlesungen über mathematische Physik*. Teubner, 233–250.
- V. V. Kozlov and S. M. Ramodanov. 2001. The Motion of a Variable Body in an Ideal Fluid. *J. Appl. Math. Mech.* 65, 4 (2001), 579–587.
- Philip V. Kulwicki and Edward J. Schleier. 1962. *Weightless Man: Self-Rotation Techniques*. Technical Report AMRL-TDR-62-129. Beh. Sci. Lab., Wright-Patterson AFB.
- V. M. Kuznetsov, B. A. Lugovtsov, and Y. N. Sher. 1967. On the Motive Mechanism of Snakes and Fish. *Arch. Rat. Mech.* 25 (1967), 367–387.
- L. D. Landau and E. M. Lifshitz. 1976. *Mechanics* (third ed.). Course of Theoretical Physics, Vol. 1. Butterworth Heinemann.
- Eric Lauga and Thomas R. Powers. 2009. The Hydrodynamics of Swimming Microorganisms. *Rep. Prog. Phys.* 72, 096601 (2009), 36pp.
- Michael Lentine, Jon Tomas Gretarsson, Craig Schroeder, Avi Robinson-Mosher, and Ronald Fedkiw. 2011. Creature Control in a Fluid Environment. *IEEE Trans. Vis. Comp. Graph.* 17, 5 (2011), 682–693.
- P. Liljeback, Ky. Y. Pettersen, Ø. Stavdahl, and J. T. Gravdahl. 2012. A Review on Modeling, Implementation, and Control of Snake Robots. *Rob. Aut. Syst.* 60, 1 (2012), 29–40.
- M. Marey. 1894. Photographs of a Tumbling Cat. *Nature* 51 (1894), 80–81.
- Jerrold E. Marsden and Matthew West. 2001. Discrete Mechanics and Variational Integrators. *Act. Num.* 10 (May 2001), 357–514.
- Gavin S. Miller. 1988. The Motion Dynamics of Snakes and Worms. In *Proc. ACM/SIGGRAPH Conf.* ACM, 169–173.
- Sehee Min, Jungdam Won, Seunghwan Lee, Jungnam Park, and Jehee Lee. 2019. SoftCon: Simulation and Control of Soft-Bodied Animals with Biomimetic Actuators. *ACM Trans. Graph.* 38, 6 (2019), 208:1–12.
- R. Montgomery. 1993. *Dynamics and Control of Mechanical Systems: The Falling Cat and Related Problems*. Number 1 in Fields Inst. Commun. Fields Institute, Chapter Gauge Theory of the Falling Cat, 193–218.

- Emmy Noether. 1918. Invariante Variationsprobleme. *Nachr. König. Ges. Wiss. Math. Phys. Klasse* (1918), 235–257. Engl. translation <https://arxiv.org/abs/physics/0503066>.
- Jim Ostrowski and Joel Burdick. 1998. The Geometric Mechanics of Undulatory Robotic Locomotion. *I. J. Rob. Res.* 17, 7 (1998), 683–701.
- Marcel Padilla, Albert Chern, Felix Knöppel, Ulrich Pinkall, and Peter Schröder. 2019. On Bubble Rings and Ink Chandeliers. *ACM Trans. Graph.* 38, 4 (2019), 129:1–14.
- Louis Poinsot. 1851. *Théorie Nouvelle de la Rotation des Corps*. Bachelier.
- E. M. Purcell. 1977. Life at Low Reynolds Number. *Amer. J. Phys.* 45, 3 (1977), 3–11.
- Michel Rieuord. 2015. *Fluid Dynamics: An Introduction*. Springer.
- Perrin E. Schiebel, Jennifer M. Reiser, Alex M. Hubbard, Lillian Chen, D. Zeb Rocklin, and Daniel I. Goldman. 2019. Mechanical Diffraction Reveals the Role of Passive Dynamics in a Slithering Snake. *Proc. Nat. Acad. Sci.* 116, 11 (2019), 4798–4803.
- Alfred Shapere and Frank Wilczek. 1989a. Geometry of Self-Propulsion at Low Reynolds Number. *J. Fluid Mech.* 198 (1989), 557–585.
- Alfred Shapere and Frank Wilczek. 1989b. Gauge Kinematics of Deformable Bodies. *Amer. J. Phys.* 57, 6 (1989), 514–518.
- Hon. J. W. Strutt, M. A. (Lord Rayleigh). 1871. Some General Theorems Relating to Vibrations. *Proc. Lond. Math. Soc.* s1-4, 1 (1871), 357–368.
- Jie Tan, Yuting Gu, Greg Turk, and C. Karen Liu. 2011. Articulated Swimming Creatures. *ACM Trans. Graph.* 30, 4 (2011), 58:1–12.
- Xiaoyuan Tu and Demetris Terzopoulos. 1994. Artificial Fishes: Physics, Locomotion, Perception, Behavior. In *Proc. ACM SIGGRAPH Conf.* 43–50.
- Steven Vogel. 1983. *Life in Moving Fluids* (2nd ed.). Princeton University Press.
- Hermann von Helmholtz. 1882. Zur Theorie der stationären Ströme in reibenden Flüssigkeiten. In *Wissenschaftliche Abhandlungen*. Vol. I. J. A. Barth, 223–230.
- Barłomiej Waszak. 2018. Limbless Movement Simulation with a Particle-Based System. *Comp. Anim. Virt. Worlds* 29, 2 (2018), 1–21.
- Steffen Weissmann and Ulrich Pinkall. 2012. Underwater Rigid Body Dynamics. *ACM Trans. Graph.* 31, 4 (2012), 104:1–7.
- Wayne L. Wooten and Jessica K. Hodgins. 1996. Animation of Human Diving. *Comp. Graph. Forum* 15, 1 (1996), 3–13.
- Jia-Chi Wu and Zoran Popović. 2003. Realistic Modeling of Bird Flight Animations. *ACM Trans. Graph.* 22, 3 (2003), 888–895.

## A MOMENTUM OF MOTION TRAJECTORIES

The energy  $\mathcal{E}$  of a curve  $\gamma: [a, b] \rightarrow M$  in a Riemannian manifold  $M$  is given by

$$\mathcal{E}(\gamma) = \frac{1}{2} \int_a^b |\gamma'|^2.$$

We are interested in the critical points of  $\mathcal{E}$  under variations that do not change  $\gamma$  except for a group of isometries.

Suppose there is a Lie group  $G$  acting on  $M$  by isometries, so that  $M$  is fibered into orbits of  $G$  with projector  $\pi: M \rightarrow M/G$ . Accordingly the tangent bundle  $TM$  splits into the *vertical space*  $V = \ker d\pi$  and the *horizontal space*  $H = V^\perp$ ,

$$TM = V \oplus H.$$

In this situation, vertical (infinitesimal) variations  $\dot{\gamma}$  belong to finite variations of  $\gamma$  that fix the image  $\pi(\gamma)$ .

To define the notion of *momentum* let  $\mathfrak{g} = T_{\text{Id}}G$  denote the *Lie algebra* of  $G$ . Then to every  $X \in \mathfrak{g}$  we can construct an associated vector field  $\widehat{X} \in \Gamma(TM)$  on  $M$ —if  $X = g'(0)$ , then  $\widehat{X}_p = (g \cdot p)'(0)$ , where the multiplication “.” denotes the action of  $g$  on an element of  $M$ . Now define a  $\mathfrak{g}^*$ -valued 1-form  $\mu$ . For  $\xi \in T_p M$  and  $X \in \mathfrak{g}$  let

$$\mu_\xi(X) := \langle \xi, \widehat{X}_p \rangle.$$

The 1-form  $\mu$  vanishes on the horizontal space and identifies the vertical space with the trivial bundle  $M \times \mathfrak{g}^*$ . The *momentum of a curve*  $\gamma$  is then defined as  $\mu_\gamma'$ .

**THEOREM 2.** *In the situation above:*

- (1) *A curve is a critical point of  $\mathcal{E}$  under vertical variations with fixed endpoints if and only if its momentum is constant.*
- (2) *A curve is a critical point of  $\mathcal{E}$  under all vertical variations if and only if its momentum is zero.*

**PROOF.** One direction basically follows from the well-known *first variational formula*: If  $\dot{\gamma}$  is a variation of  $\gamma$ , then

$$\dot{\mathcal{E}} = \langle \gamma', \dot{\gamma} \rangle|_a^b - \int_a^b \langle \gamma'', \dot{\gamma} \rangle.$$

Thus, in both cases, criticality implies  $\gamma'' \in H_\gamma$ . In particular, since  $G$  acts by isometries, the action leaves  $\mathcal{E}$  invariant and we get

$$0 = \dot{\mathcal{E}} = \langle \gamma', \dot{\gamma} \rangle|_a^b = \mu_{\gamma'}(b)(X) - \mu_{\gamma'}(a)(X),$$

for all  $X \in \mathfrak{g}$ . The very same computation also holds for restrictions of  $\gamma$  to any sub-interval of  $[a, b]$ . So that we can conclude that a critical curve  $\gamma$  has a constant momentum  $\mu_\gamma'$ . In case  $\gamma$  is critical under arbitrary vertical variations one finds that  $\mu_{\gamma'}(a) = 0$  by using vertical variations vanishing at  $b$ .

Conversely, suppose the momentum is constant. Then, for any  $X \in \mathfrak{g}$ , we have

$$0 = (\mu_{\gamma'}(X))' = \langle \gamma', \widehat{X}_Y \rangle' = \langle \gamma'', \widehat{X}_Y \rangle + \langle \gamma', \nabla_{\gamma'} \widehat{X} \rangle = \langle \gamma'', \widehat{X}_Y \rangle,$$

where the last equality follows from  $\nabla \widehat{X}$  being skew-adjoint for  $\widehat{X}$  a Killing vector field. Since  $G$  acts transitively on fibers we conclude that  $\gamma''$  is horizontal everywhere. In both cases, criticality now again easily follows from the first variational formula.  $\square$

## A.1 Example

To illustrate Thm. 2 consider a rigid body in Euclidean 3-space with mass  $m_j$  concentrated at finitely many points  $p_1, \dots, p_n \in \mathbb{R}^3$ . In that case  $G = \text{SE}(3)$  and the motion obeys the *principle of least action*, i.e., it is given by the critical points of

$$\mathcal{E}(\gamma) = \frac{1}{2} \int_a^b \sum_{j=1}^n m_j |\gamma'_j|^2$$

under vertical variations fixing endpoints. The Lie algebra  $\text{se}(3)$  can be identified with  $\mathbb{R}^6$ —each  $X \in \text{se}(3)$  is of the form

$$X_p = \omega \times p + v, \quad \omega, v \in \mathbb{R}^3.$$

The momentum of a curve  $\gamma$  is given by

$$\mu_{\gamma'}(X) = \sum_{j=1}^n m_j \langle \gamma'_j, \omega \times \gamma_j + v \rangle = \left\langle \sum_{j=1}^n m_j \gamma_j \times \gamma'_j, \omega \right\rangle + \left\langle \sum_{j=1}^n m_j \gamma'_j, v \right\rangle$$

consisting of two parts—the *angular momentum*  $\mathbf{l} = \sum_{j=1}^n m_j \gamma_j \times \gamma'_j$  and the *linear momentum*  $\mathbf{p} = \sum_{j=1}^n m_j \gamma'_j$  (compare to Eq. (3))—and the motion of the rigid body is determined through their constancy.

## B DISCRETE MOTION TRAJECTORIES

Now suppose that for the sake of numerical computations we want a time-discrete version of this problem. Then we are given a finite sequence of times and corresponding orbits  $M_0, \dots, M_T$ . We are looking for a sequence  $\gamma_0, \dots, \gamma_T$  of points  $\gamma_t \in M_t$  which is critical for some discrete version

$$\mathcal{E}(\gamma) = \sum_{t=1}^T E(\gamma_{t-1}, \gamma_t)$$

of the smooth energy. Here we assume  $E$  is invariant with respect to the action of  $G$ ,  $E(g \cdot \gamma_{t-1}, g \cdot \gamma_t) = E(\gamma_{t-1}, \gamma_t)$  for all  $g \in G$ . We

now define the *momentum* of the discrete curve  $\gamma$  as

$$\mu_t(X) := (d_{\gamma_{t-1}} E(., \gamma_t))(\widehat{X}_{\gamma_{t-1}}) \quad \forall X \in \mathfrak{g}. \quad (7)$$

Where  $E(., \gamma_t) : M_{t-1} \rightarrow \mathbb{R}$  and  $d_{\gamma_{t-1}} E(., \gamma_t)$  denotes its differential evaluated at  $\gamma_{t-1}$  which is then evaluated at  $\widehat{X}_{\gamma_{t-1}} \in T_{\gamma_{t-1}} M_{t-1}$ . This provides us with a discrete analogue of Thm. 2.

**THEOREM 3.** *In the situation above:*

- (1) *A discrete curve is a critical point of  $\mathcal{E}$  under vertical variations with fixed endpoints if and only if its momentum is constant.*
- (2) *A discrete curve is a critical point of  $\mathcal{E}$  under all vertical variations if and only if its momentum is zero.*

**PROOF.** Differentiating  $\mathcal{E}$  with respect to a variation  $\dot{\gamma}$  of  $\gamma$  yields

$$\dot{\mathcal{E}} = \sum_{t=1}^T (d_{\gamma_{t-1}}(E(., \gamma_t))(\dot{\gamma}_{t-1}) + d_{\gamma_t}(E(\gamma_{t-1}, .))(\dot{\gamma}_t)).$$

By the symmetry of  $E$ , if  $g$  is a curve in  $G$  with  $g'(0) = X \in \mathfrak{g}$ , then

$$\begin{aligned} 0 &= E(g \cdot \gamma_{t-1}, g \cdot \gamma_t)'(0) = (d_{(g \cdot \gamma_{t-1}, \gamma_t)} E)(\widehat{X}_{\gamma_{t-1}}, \widehat{X}_{\gamma_t}) \\ &= (d_{(\gamma_{t-1}, \gamma_t)} E)(\widehat{X}_{\gamma_{t-1}}, 0) + (d_{(\gamma_{t-1}, \gamma_t)} E)(0, \widehat{X}_{\gamma_t}), \end{aligned}$$

where we identified  $T_{(\gamma_{t-1}, \gamma_t)}(M_{t-1} \times M_t) = T_{\gamma_{t-1}} M_{t-1} \oplus T_{\gamma_t} M_t$ , which implies

$$(d_{\gamma_t} E(\gamma_{t-1}, .))(\widehat{X}_{\gamma_t}) = -(d_{\gamma_{t-1}} E(., \gamma_t))(\widehat{X}_{\gamma_{t-1}}) = -\mu_t(X).$$

For vertical  $\dot{\gamma}$  there are  $X_t \in \mathfrak{g}$  such that  $\dot{\gamma}_t = \widehat{X}_t \gamma_t$ , i.e., the tangent vector field  $\widehat{X}_t$  on  $M_t$  evaluated at the foot point  $\gamma_t$ . Thus, we obtain

$$\begin{aligned} \dot{\mathcal{E}} &= \sum_{t=1}^T (d_{\gamma_{t-1}}(E(., \gamma_t))(\widehat{X}_{\gamma_{t-1}}) + d_{\gamma_t}(E(\gamma_{t-1}, .))(\widehat{X}_{\gamma_t})) \\ &= \sum_{t=1}^T (\mu_t(X_{t-1}) - \mu_t(X_t)). \end{aligned}$$

Reordering for  $X_t$  yields

$$\dot{\mathcal{E}} = \mu_1(X_0) - \mu_T(X_T) + \sum_{t=1}^{T-1} (\mu_{t+1} - \mu_t)(X_t). \quad (8)$$

From this both claims follow.  $\square$

A straightforward corollary to Thm. 3 provides a practical algorithm for time stepping by solving a sequence of non-linear root finding problems:

**COROLLARY 1.** *Let  $\mu_0 \in \mathfrak{g}^*$  and suppose we determine a sequence  $\gamma = (\gamma_0, \dots, \gamma_T)$  by starting with an arbitrary  $\gamma_0 \in M_0$ , then find  $\gamma_1 \in M_1$  by solving  $\mu_1 = \mu_0$  and so on. Then  $\gamma$  is a critical point of  $\mathcal{E}$  under vertical variations fixing endpoints. If  $\mu_0 = 0$ , then the sequence is critical with respect to arbitrary vertical variations.*

## C DISCRETE EULER-LAGRANGE EQUATIONS

The placement of the shapes is characterized by the energy being critical under all vertical variations. To this end we need to compute variations of the two point energy  $E(\gamma_{t-1}, \gamma_t)$  (Eq. (4)) with respect to rigid motion of the shape at the beginning of the time interval (App. B), i.e., in the first slot of  $E$

$$\dot{E}(\gamma_{t-1}, \gamma_t) = \left\langle \frac{1}{2} \dot{B}^{\gamma_{t-1}} \Delta p^t, \Delta p^t \right\rangle - \left\langle (B^{\gamma_t} + B^{\gamma_{t-1}}) \Delta p^t, \dot{p}^{t-1} \right\rangle. \quad (9)$$

Now consider an arbitrary infinitesimal Euclidean motion  $\dot{g}_{t-1} \in \text{se}(3)$ , and denote by  $\omega$  and  $b$  the rotational and translational components, i.e.,  $\dot{g}_{t-1}(x) = \omega \times x + b$ .

Variations due to infinitesimal translations follow easily since  $\dot{B}^{\gamma_{t-1}} = 0$  when  $\omega = 0$ , eliminating the first term of Eq. (9). This leaves us with  $\dot{p}_j^{t-1} = b$  for all  $j$  and

$$\dot{E}(\gamma_{t-1}, \gamma_t) = \left\langle - \sum_{j=1}^n ((B^{\gamma_t} + B^{\gamma_{t-1}}) \Delta p^t)_j, b \right\rangle_{\mathbb{R}^3}.$$

For an infinitesimal rotation ( $b = 0$ ) the first term in Eq. (9) can be computed geometrically by using the SE(3) symmetry of our setup. Let  $\Omega \in \mathbb{R}^{3n \times 3n}$  be block diagonal with all blocks equal to the cross product matrix  $\omega \times \in \mathbb{R}^{3 \times 3}$ , and let  $A_\tau := \exp(\tau \Omega)$  be the resulting rotation of  $\mathbb{R}^{3n}$ . If we rotate  $\gamma_{t-1}$  accordingly to obtain  $\gamma_{t-1}^\tau := A_\tau \gamma_{t-1}$  then the SE(3) symmetry implies that for any vector  $\dot{\gamma} \in \mathbb{R}^{3n}$

$$\langle B^{\gamma_{t-1}} A_\tau \dot{\gamma}, A_\tau \dot{\gamma} \rangle = \langle B^{\gamma_{t-1}} \dot{\gamma}, \dot{\gamma} \rangle.$$

It follows that  $B^{\gamma_{t-1}} = A_\tau^\top B^{\gamma_{t-1}} A_\tau$ , and by differentiating at  $\tau = 0$  we deduce that

$$\dot{B}^{\gamma_{t-1}} = [\Omega, B^{\gamma_{t-1}}] = \Omega B^{\gamma_{t-1}} - B^{\gamma_{t-1}} \Omega.$$

Plugging this back into the first term of Eq. (9) gives

$$\left\langle \frac{1}{2} [\Omega, B^{\gamma_{t-1}}] \Delta p^t, \Delta p^t \right\rangle = -\langle B^{\gamma_{t-1}} \Delta p^t, \Omega \Delta p^t \rangle,$$

using the skew-symmetry of  $\Omega$  and the symmetry of  $B^{\gamma_t}$ . Since  $\dot{p}^{t-1} = \Omega p^{t-1}$ , we find that the second term of Eq. (9) equals

$$-\left\langle (B^{\gamma_t} + B^{\gamma_{t-1}}) \Delta p^t, \Omega p^{t-1} \right\rangle.$$

Taken together the energy variation induced by an infinitesimal rotation  $\omega$  is

$$\dot{E}(\gamma_{t-1}, \gamma_t) = -\left\langle B^{\gamma_{t-1}} \Delta p^t, \Omega p^t \right\rangle - \left\langle B^{\gamma_t} \Delta p^t, \Omega p^{t-1} \right\rangle$$

which simplifies to

$$\dot{E}(\gamma_{t-1}, \gamma_t) = -\left\langle \sum_{j=1}^n p_j^t \times (B^{\gamma_{t-1}} \Delta p^t)_j + p_j^{t-1} \times (B^{\gamma_t} \Delta p^t)_j, \omega \right\rangle_{\mathbb{R}^3}.$$

We collect the terms paired with  $\omega$  and  $b$  into  $\mu_t \in \text{se}(3)^* \equiv \mathbb{R}^6$

$$\mu_t := \begin{pmatrix} -\sum_j p_j^t \times (B^{\gamma_{t-1}} \Delta p^t)_j + p_j^{t-1} \times (B^{\gamma_t} \Delta p^t)_j \\ -\sum_j ((B^{\gamma_t} + B^{\gamma_{t-1}}) \Delta p^t)_j \end{pmatrix}$$

and will refer to it as the *discrete momentum* to mirror the general setup in App. B and in particular Eq. (7).